

Constraining the geometry of the nuclear wind in PDS 456 using a novel emission model

A. Luminari^{1,2,3}, E. Piconcelli², F. Tombesi^{1,4,5}, L. Zappacosta², F. Fiore⁶, L. Piro⁷, F. Vagnetti¹

¹ Department of Physics, University of Rome “Tor Vergata”, Via della Ricerca Scientifica 1, I-00133 Rome, Italy

² INAF Rome Astronomical Observatory, Via Frascati 33, 00078 Monteporzio Catone, Italy

³ Department of Physics, University of Rome “Sapienza”, Piazzale Aldo Moro 5, I-00185, Rome, Italy

⁴ Department of Astronomy, University of Maryland, College Park, MD 20742, USA

⁵ X-ray Astrophysics Laboratory, NASA/Goddard Space Flight Center, Greenbelt, MD 20771, USA

⁶ INAF Trieste Astronomical Observatory, Via G. B. Tiepolo 11, I-34143 Trieste, Italy

⁷ INAF Istituto di Astrofisica e Planetologia Spaziali, via Fosso del Cavaliere 100, I-00133 Rome, Italy

Received June 12, 2018; accepted September 06, 2018

ABSTRACT

Context. Outflows from active galactic nuclei (AGN) are often invoked to explain the co-evolution of AGN and their host galaxies, and the scaling relations between the central black hole mass and the bulge velocity dispersion. Nuclear winds are often seen in the X-ray spectra through Fe K shell transitions and some of them are called ultra fast outflows (UFOs) due to their high velocities, up to some fractions of the speed of light. If they were able to transfer some percentage of the AGN luminosity to the host galaxy, this might be enough to trigger an efficient feedback mechanism.

Aims. We aim to establish new constraints on the covering fraction and on the kinematic properties of the UFO in the powerful ($L_{bol} \sim 10^{47}$ erg/s) quasar PDS 456, an established Rosetta stone for studying AGN feedback from disk winds. This will allow us to estimate the mass outflow rate and the energy transfer rate of the wind, which are key quantities to understand the potential impact on the host galaxy.

Methods. We analyze two sets of simultaneous XMM-Newton and NuSTAR observations taken in September 2013 and reported in Nardini et al. (2015) as having similar broadband spectral properties. We fit the Fe K features with a P-Cygni profile between 5 and 14 keV, using a novel Monte Carlo model for the WIND Emission (WINE).

Results. We find an outflow velocity ranging from 0.17 to 0.28 c, with a mean value of 0.23 c. We obtain an opening angle of the wind of 71_{-8}^{+13} deg and a covering fraction of $0.7_{-0.3}^{+0.2}$, suggesting a wide-angle outflow. We check the reliability of the WINE model by performing extensive simulations of joint XMM-Newton and NuSTAR observations. Furthermore, we test the accuracy of the WINE model in recovering the geometrical properties of UFOs by simulating observations with the forthcoming Advanced Telescope for High-Energy Astrophysics (ATHENA) in the X-ray band.

Key words. quasars: supermassive black holes – X-rays: galaxies – line: profiles – techniques: spectroscopic – quasars: emission lines – galaxies: active

1. Introduction

Accretion disk winds are believed to play a fundamental role in the feedback from active galactic nuclei (AGN) to their host galaxy. Both theoretical and observational evidences show that they are potentially able to transfer a significant fraction of the AGN’s power (Di Matteo et al. 2005), up to $\sim 3 - 5\%$ L_{AGN} (King & Pounds 2015, Tombesi et al. 2015, Feruglio et al. 2015, Bischetti et al. 2017, Fiore et al. 2017). This amount of energy could overcome the binding energy of the host galaxy, and is often invoked to explain the observed relation between the supermassive black hole (SMBH) mass and the bulge velocity dispersion (the “ $M - \sigma$ ” relation, see e.g., Kormendy & Ho 2013). According to the most accepted scenario (see, e.g., King & Pounds 2015), the gas is accelerated at accretion disk scales, propagates towards the host galaxy, and impacts the interstellar matter (ISM), producing a shock front (Zubovas & King 2012, Faucher-Giguère & Quataert 2012). If the kinetic energy is conserved during this process, the shocked gas may drive a massive, galaxy-scale outflow, with mass transfer rates up to $\sim 10^3 M_{\odot} \text{ yr}^{-1}$ and velocities = 1000 km s^{-1} .

In this two-phase scenario, the covering fraction of the disk wind, C_f , together with its velocity, density, and launching radius, are fundamental quantities to understand the amount of momentum and energy deposited into the ISM. The accurate measurement of these quantities is crucial to reliably constrain the role of the disk winds in the co-evolution of AGN and their host galaxies.

In this paper, we present the application of our novel model of AGN wind emission (WINE) to the broadband XMM-Newton+NuSTAR spectrum of PDS 456. This nearby ($z = 0.184$) luminous quasar exhibits the prototype of an ultra fast outflow (UFO) traced by a P-Cygni feature, due to highly-ionized Fe, with a ionization parameter $\xi = \frac{L_{ion}}{nR^2} \sim 10^5 \text{ erg cm s}^{-1}$, where L_{ion} is the luminosity in the 1-1000 Rydberg interval ($1Rd = 13.6 \text{ eV}$), n is the gas number density, and R is the distance from the ionizing source. The outflow velocity is $\sim 0.25c$ and the launching radius is $< 200 r_g$ ¹ (Reeves et al. 2003, Nardini et al. 2015, hereafter N15). N15 inferred a C_f of

¹ The gravitational radius r_g is defined as $r_g = GM/c^2$, with G the gravitational constant and M the black hole mass.

the UFO of $0.8 (= 3.2\pi)$ and a kinetic power of $\sim 20\%$ of the bolometric luminosity of the quasar. These estimates are based on a spectral fitting using XSTAR tables (Kallman & Bautista 2001) to model both UFO emission and absorption features, in which the outflowing gas is approximated as a spherical shell with constant radial velocity.

The present paper is organized as follows. In Sect. 2 we describe the wind model. In Sect. 3 we present the X-ray data analysis and the results of the spectral fitting obtained by applying our model. Section 4 is devoted to the discussion of our findings, with particular emphasis on C_f and the velocity of the outflow, the derived mass and energy transfer rates, and their implications for AGN feedback.

2. The Wind Emission (WINE) model

In the WINE model the wind is approximated as a conical region, with the vertex centered on the SMBH, the same symmetry axis as the accretion disk, and the gas velocity directed radially outward. This conical shape is consistent with the most popular accretion disk wind simulations (e.g., Proga & Kallman 2004, Fukumura et al. 2010, Oshuga et al. 2009). As the UFOs originate from the innermost region of the accretion disk, we consider that the rear cone is not observable (see Fig. 1).

The free parameters of the model are the opening angle of the cone (i.e., θ_{out} in Fig. 1), the inclination angle i of the line of sight (LOS) with respect to the symmetry axis, the maximum velocity of the wind (v_{max}), and the deceleration factor of the wind radial velocity (s). The radial velocity of the wind is defined as

$$v(r') = v_{max}(1 - sr'), \quad (1)$$

where $r' \equiv \frac{r}{r_{cone}}$ and r_{cone} is the height of the cone. Equation 1 represents a first-order expansion of the velocity with respect to r and provides a basic description of the wind kinematic.² Given the observed UFO absorption feature, we require that $i < \theta_{out}$, that is, that the LOS has to lie inside the wind. We also consider a more refined version of the model, allowing for an internal cavity with variable angular aperture θ_{in} .

The conical geometry of the wind is approximated by a large number l (i.e., 100) of conical shells, equally spaced between $r = 0$ and $r = r_{cone}$. These shells have angular opening θ_{out} with respect to the symmetry axis. For each shell, we assign angular coordinates to a number n of points ($n = 10^4$ by default) through a Monte Carlo method. The radial velocity is a function of radius, according to the linear relation of Eq. 1, in which s ranges from 0 to 1 and represents the deceleration factor of the wind as a function of r' , which is the distance from the vertex normalized to the height of the cone (r_{cone}). The latter is not a parameter of the WINE model, as in Eq. 1 the radial velocity only depends on the dimensionless radius $r' \equiv r/r_{cone}$ spanning the range $[0, 1]$. Accordingly, the radial velocity of the wind at the vertex is v_{max} , while the velocity at $r = r_{cone}$ is defined as v_{min} .

We assume the same intrinsic brightness B_{int} for each point all over the cone (see Eq. 3 and following discussion). Then, using special relativity, we calculate for each point of the shell the projected value of B_{int} and $v(r)$ along the LOS: B_{proj} and $v(r)_{proj}$, respectively. Values of B_{proj} are then grouped into bins of $3,600 \text{ km s}^{-1}$. In this way we obtain the spectrum of a single

² We are aware that the velocity profile of the wind may differ from the one we are assuming here. Specifically, the wind may be accelerated by radiation pressure or MHD driving, showing a non-linear dependence both on the radius r and on the azimuthal angle with respect to the accretion disk. We will check these dependences in a forthcoming work.

shell. The combination of each shell spectrum at all radii (i.e., from $r = 0$ to $r = r_{cone}$) provides the global spectrum emitted by the wind.

The total observed emissivity of the wind is therefore $B_{tot} = \sum_{l=1}^{100} \sum_{n=1}^{10^4} B_{proj}$ and parametrized in *xspec* through the normalization of the WINE model component (see Sect. 3). Notwithstanding the fact that B_{int} can be estimated from B_{tot} , it is not possible to derive from it a reliable value for the Fe ions' emissivity, given the current stage of the WINE model, which would allow us to infer the column density of the wind. This would require an accurate treatment of the ionic abundances and emissivities, as well as the photoionization equilibrium and radiative transfer within the medium. This will be accounted for in a future version of the WINE model by incorporating XSTAR tables into the present modelization of the wind (see Sect. 4).

Our model assumes a radial density profile of the wind $\rho \propto r^\alpha$. In the case of the UFO in PDS 456, we choose $\alpha = -2$, an isothermal density profile. This ensures that the ionization parameter as a function of the radius of the wind, $\xi(r)$, is constant at all radii, in accordance with the observations of PDS 456 showing that the wind ionization is dominated by Fe XXVI (Reeves et al. 2003, Reeves et al. 2009, N15). In fact, the number density of the wind can be written as

$$n(r) = n_0 \left(\frac{r_0}{r} \right)^2, \quad (2)$$

where n_0 is the density of the wind at a fiducial radius r_0 . Using Eq. 2, $\xi(r)$ can be expressed as

$$\xi = \frac{L_{ion}}{n(r)r^2} = \frac{L_{ion}}{n_0 r_0^2}, \quad (3)$$

where there is no dependence on r . A constant ξ , as shown in Eq. 3, indicates that the relative abundance of the ions, including Fe XXVI, is roughly constant within the medium and therefore justifies our assumption of constant B_{int} .

In the following we provide a detailed description of the free parameters of the WINE model:

- v_{max} : the maximum velocity of the wind (in units of c) corresponding to the starting velocity at the vertex of the cone. We assume $[0.1c, 0.6c]$ as the possible range of v_{max} and we span this interval with a resolution of 0.01c.
- The opening angle θ_{out} can range from 0 to 90 deg (see Fig. 1). This interval is sampled by nine equally-space steps of 10 deg.
- i : the upper limit of this parameter is set by the requirement of having an LOS inside the cone aperture, that is, $i \leq \theta_{out}$. The possible range for i , $[0, \theta_{out}]$, is sampled with 11 equally spaced steps.
- The deceleration factor of the wind s (Eq. 1) ranges from 0 to 1 and it is sampled through steps of 0.1.
- Furthermore, an inner cavity in the cone can be accounted for by an additional parameter θ_{in} , which represents the angular amplitude with respect to the symmetry axis. Parameter θ_{in} can span the open interval $(0, i)$.

From this set of free parameters, it is possible to derive (i) $v(r)$, as defined by Eq. 1, and (ii) C_f , the covering factor of the wind defined as the fraction of sky covered by the cone, as seen from the vertex:

$$C_f = 1 - \cos(\theta_{out}). \quad (4)$$

In the case of a cone with an inner cavity, Eq. 4 becomes

$$C_f = \cos(\theta_{in}) - \cos(\theta_{out}). \quad (5)$$

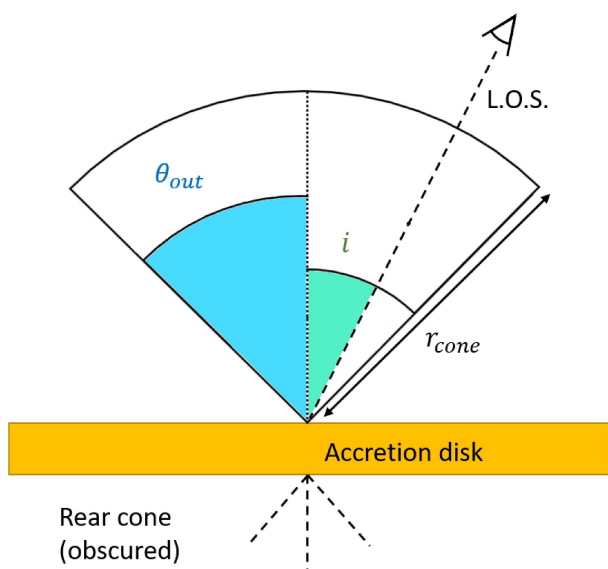


Fig. 1: Sketch of the WINE model. Further details can be found in Sect. 2.

3. Spectral analysis

We merge the simultaneous XMM-Newton+NuSTAR spectra from Epoch 3 (September 15, 2013) and Epoch 4 (September 20, 2013) in N15 (see Table 1) in order to increase the signal-to-noise ratio. We consider these two datasets since they are virtually indistinguishable in terms of flux and spectral shape.

Data reduction and spectral extraction are performed using the data analysis software SAS 16.0.0 and NUSTARDAS v1.7.1 (calibration database version 20170222) for XMM-Newton and NuSTAR, respectively. Table 1 lists the journal of the observations. We adopt the same filtering scheme and spectral extraction regions as in N15.

We co-add the spectra of Epochs 3 and 4, both for XMM-Newton and for NuSTAR, using the *ftools* task *addascaspec*, and finally group them to a minimum of 100 and 50 counts per energy bin, respectively. We base our fitting procedure on that of N15, with a lower energy bound of 3 keV. This allows us to avoid two complex spectral features: the soft excess at energies below ~ 1 keV and the warm absorber at $\lesssim 2$ keV. The upper bounds are 10 and 30 keV for the XMM-Newton and NuSTAR spectra, respectively. The spectra are always jointly fitted, with an intercalibration constant left free to vary.

3.1. Phenomenological fit

Similarly to N15, we first perform a preliminary fit to describe the continuum emission using a power law modified by a neutral partial covering absorber, responsible for the spectral curvature below 4 keV. We ignore the energy interval around the Fe K shell features, from 5 and 14 keV. Using directly the *xspec* notation, the fitting model can be expressed by the analytical expression

$$\text{constant} * \text{phabs} * \text{zpcfabs} * \text{zpowerlaw}, \quad (6)$$

where *constant* is a constant multiplicative factor, set $\equiv 1$ for XMM-Newton data and left free to vary for the two NuSTAR modules. This is necessary to account for intercalibration differences between the three instruments. Galactic absorption is represented through *phabs*, which is set to $N_H^{\text{Gal}} \equiv 2 \times 10^{21} \text{ cm}^{-2}$

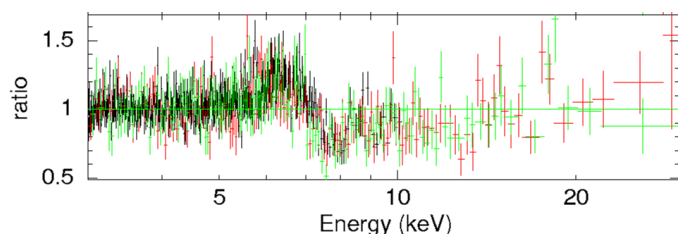


Fig. 2: Ratio between data and the best-fit continuum model to the 3-5 keV + 15-30 keV spectrum, once the 5-14 keV region is included (see Sect. 3.1 for details). Black, green, and red crosses indicate XMM-Newton/pn, NuSTAR FPMA, and FPMB data.

(see N15). The neutral partial covering absorber is described by *zpcfabs*. Finally, the spectral index Γ and normalization K of the power-law continuum are left free to vary. We obtain a spectral index $\Gamma = 2.40 \pm 0.06$ for the continuum component. For the absorber, we find a column density of $N_H = 2.4 \pm 0.3 \times 10^{23} \text{ cm}^{-2}$ and covering fraction of $C_f = 0.42 \pm 0.05$, suggesting a more distant feature from the AGN with respect to the UFO. These findings are in agreement with the low values for N_H and ξ and the low variability found in N15 for this component. The resulting χ^2 is 309 for 362 degrees of freedom. Table 2 shows the best-fit parameters. Figure 2 shows the residuals in terms of data-to-model ratios over the 3-30 keV band.

Then, in order to have a first description of the absorption and emission features related to the Fe K shell, we consider the whole energy band adding a Gaussian emission line with energy corresponding to Fe XXVI Ly α ($E = 6.97$ keV rest frame) and free width and redshift. We model the absorption including two Gaussian lines for Fe XXVI Ly α and Ly β ($E = 8.25$ keV rest frame) and a photoelectric edge at $E = 9.28$ keV rest frame, to take into account the K shell edge from Fe XXVI.

The inclusion of these spectral components is based on the phenomenological analysis reported in N15, in order to fully characterize the observed Fe K spectral features. The resulting model is

$$\text{constant} * \text{phabs} * (\text{zpcfabs} * \text{zedge} * \text{zpowerlaw} + \text{zgauss}_{em_Ly\alpha} + \text{zgauss}_{abs_Ly\alpha} + \text{zgauss}_{abs_Ly\beta}). \quad (7)$$

In addition to the components in expression 6, *zgauss_{em}Ly α* indicates the Gaussian emission associated to Fe XXVI Ly α and *zgauss_{abs}Ly α* , *zgauss_{abs}Ly β* represents the Gaussian absorption for Ly α and Ly β lines, respectively. The term *zedge* corresponds to the photoelectric edge due to the Fe K shell.

A simple fit leaving all the parameters free returns an almost identical redshift for both the absorption lines, $z = -0.100 \pm 0.009$, -0.107 ± 0.005 , for Ly α and Ly β , respectively, corresponding to a blueshifted velocity of $\approx 0.26, 0.27c$, while the redshift of the K shell edge, $z = -0.071 \pm 0.1$, implies a velocity of $\approx 0.24c$. Since we expect that the same medium is responsible for all the absorption features, we impose the same redshift for the lines and the edge. Moreover, we link the Gaussian line widths in order to have the same velocity dispersion. Table 3 lists the best-fit values for these emission and absorption components, obtained by keeping the continuum and the partial covering absorption parameters fixed to the values shown in Table 2. The best-fit results in a $\chi^2 = 649$ for 705 degrees of freedom (d.o.f.), confirming the validity of our hypothesis.

Interestingly, the redshift of the emitting component is significantly shifted with respect of that of the host galaxy: $z = 0.117$ versus $z = 0.184$. This corresponds to a difference in terms

Epoch	Telescope	Obs. ID	Date and time	T_{tot} (ks) ^(a)	Instrument	T_{net} (ks) ^(b)	Net counts (k) ^(c)	Extraction ^(d)
3	XMM	0721010501	2013-09-15 18:30:00	120.5	pn	102.2	207.6	35/60
	NuSTAR	60002032006	2013-09-15 17:56:07	119.1	FPMA	44.0	4.3	80/80
					FPMB	44.0	4.0	80/80
4	XMM	0721010501	2013-09-20 02:29:39	112.1	pn	94.9	188.5	35/60
	NuSTAR	60002032008	2013-09-20 03:06:07	113.8	FPMA	58.5	5.9	80/80
					FPMB	58.5	5.7	80/80

Table 1: Journal of the observations. (a), (b) Observation lengths, in ks, before and after filtering, respectively. (c) Net counts in units of 10^3 photons in the 3-10(30) keV band for XMM-Newton(NuSTAR). (d) Extraction regions for source and/or background in arcsec.

Parameter	Value
constant ^(a)	$1^{(f)}$, 1.07 ± 0.02 , 1.08 ± 0.02
phabs	
N_H	$0.2^{(f)} \times 10^{22} \text{ cm}^{-2}$
zpcfabs	
N_H	$24_{-9}^{+8} \times 10^{22} \text{ cm}^{-2}$
$f_{cov}^{(b)}$	$0.42_{-0.04}^{+0.05}$
zpowerlaw	
Γ	2.40 ± 0.07
$K^{(c)}$	$5.4_{-1.0}^{+1.3}$
z	$0.184^{(f)}$
$\chi^2/\text{d.o.f.}$	309/362

Table 2: Best-fit values for the continuum fitting (see relation 6). Hereafter, errors are at 68% c.l.. (a) *constant* has three values because is the only parameter allowed to vary between the different datasets (values shown for XMM-Newton pn and NuSTAR FPMA and FPMB, respectively). (b) f_{cov} is the covering fraction of the intrinsic cold absorber. (c) Normalization in units of 10^{-3} photons $\text{keV}^{-1} \text{ cm}^{-2} \text{ s}^{-1}$ at 1 keV. (f) Fixed value.

Parameter	Value
zedge	
<i>Edge En.</i> (keV)	$9.28^{(f)}$
$f^{(a)}$	0.19 ± 0.04
$z^{(b)}$	$-0.096_{-0.007}^{+0.008}$
zgauss_em	
<i>En.</i> (keV)	$6.97^{(f)}$
σ (keV)	0.7 ± 0.1
z	$0.12_{-0.02}^{+0.01}$
$K^{(c)}$	11_{-1}^{+2}
zgauss_Lyα	
<i>En.</i> (keV)	$6.97^{(f)}$
$\sigma^{(d)}$ (keV)	0.33 ± 0.04
$z^{(b)}$	$-0.096_{-0.007}^{+0.008}$
$K^{(c)}$	$5.8_{-0.1}^{+0.6}$
zgauss_Lyβ	
<i>En.</i> (keV)	$8.25^{(f)}$
$\sigma^{(d)}$ (keV)	0.39 ± 0.05
$z^{(b)}$	$-0.096_{-0.007}^{+0.008}$
$K^{(c)}$	2.6 ± 0.4
$\chi^2/\text{d.o.f.}$	649/705

Table 3: Best-fit values for the phenomenological fit (see relation 7). (a) f is defined as the absorption depth at threshold. (b) Linked values. (c) Gaussian function normalization K is in units of 10^{-6} photons $\text{cm}^{-2} \text{ s}^{-1}$. (d) Linked values. (f) Fixed value.

of blue-shifted velocity along the LOS of $\approx 0.06c$ ($\sim 18,000 \text{ km s}^{-1}$), lending support to the idea that we are observing the approaching component of the biconical outflow as in Fig. 1.

3.2. Fit with the WINE model

As a further step, we replace the Gaussian emission line of the phenomenological fit with two WINE model components, corresponding to Ly α and Ly β emission. The continuum and neutral partial covering absorber are still parametrized as in Sect. 3.1.

The fitting model is described by the expression

$$\begin{aligned} & \text{constant} * \text{phabs} * (\text{zpcfabs} * \text{smedge} * \text{zpowerlaw} \\ & + \text{WINE_Ly}\alpha + \text{WINE_Ly}\beta + \text{zgauss_Ly}\alpha + \text{zgauss_Ly}\beta), \end{aligned} \quad (8)$$

where *WINE_Ly α* and *WINE_Ly β* represent the two WINE model emission components. The two Gaussian absorption lines, *zgauss_Ly α* and *zgauss_Ly β* , account for Ly α and Ly β absorption, respectively, and *smedge* (Ebisawa et al. 1994) is a smeared photoelectric edge, to account for the velocity gradient of the wind (see Eq. 1). *WINE_Ly α* and *WINE_Ly β* have identical parameters, except for rest-frame energy and normalization. Specifically, the ratio between the normalizations corresponds to the ratio of the oscillator strength of Fe XXVI Ly α and Ly β (Molendi et al. 2003, Tombesi et al. 2011).

Since we expect that both the emission and absorption features are due to the same medium, we tie the redshift and broadening of *zgauss_Ly α* , *zgauss_Ly β* , and *smedge* to the emission parameters in the WINE model. Specifically, since our LOS intercepts the UFO, the velocity component of the gas along the LOS (i.e., the gas responsible for the absorption) coincides with the radial velocity $v(r)$. So, the average redshift z_{avg} of *zgauss_Ly α* , *zgauss_Ly β* and *smedge* corresponds to the average outflow velocity, $v_{avg} \equiv v(r_{cone}/2)$, according to the equation

$$z_{avg} = \frac{1 + z_{PDS}}{\sqrt{(1 + v_{avg})/(1 - v_{avg})}} - 1, \quad (9)$$

where $z_{PDS} = 0.184$. Moreover, we assume that the standard deviation σ of *zgauss_Ly α* and *zgauss_Ly β* is dominated by the velocity shear of the wind. Hence, we set σ , in terms of velocity, equal to the difference $v_{max} - v_{avg}$, while in terms of energy it can be expressed as

$$\sigma = E * \left(\frac{1}{1.184 \sqrt{(1 - v_{max})/(1 + v_{max})}} - \frac{1}{1 + z_{avg}} \right), \quad (10)$$

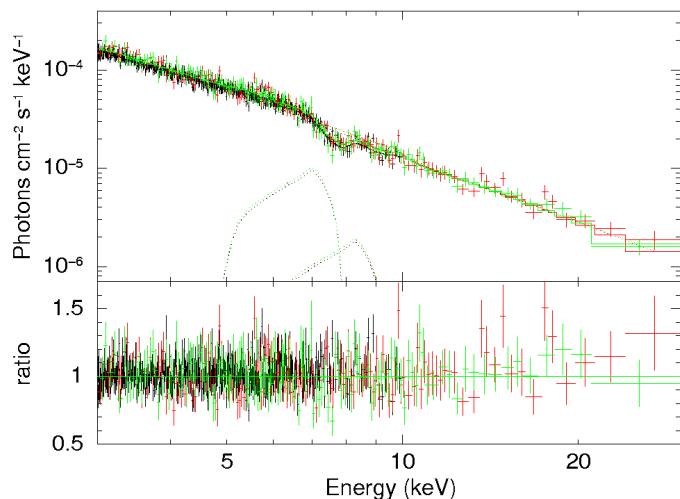


Fig. 3: Top panel: data (symbols as in fig 2) and best-fit model (solid line) including two WINE model components (dotted lines). Bottom panel: ratios between data and best fit model. See Sect. 3.2 for more details.

where E is the rest frame line energy. The same formula, using the photoionization energy threshold, can be used to express the smearing characteristic width in the *smedge* component.

Figure 3 shows the result of the fit assuming a full cone (without inner cavity). The associated χ^2 (dof) is 652 (715). The best-fit values are listed in Table 4. The radial velocity $v(r)$ ranges from $\approx 0.28c$ to $\approx 0.17c$. Regarding the outflow geometry, we obtain $\theta_{out} \sim 70$ deg, $i \sim 60$ deg, and a covering fraction (calculated as the fraction of visible hemisphere covered by the wind) of $C_f \sim 0.7$.

We also evaluate the inclusion of the cavity and find that it is not statistically required by the data, with a poorly constrained value of θ_{in} , with an upper limit of 21 deg (90% *c.l.*).

3.3. Reliability of the WINE model

We perform extensive simulations in order to check the reliability of the WINE model. In particular here we present two cases. We first use as input our best-fit values (see Sect. 3.2 and Table 4) and simulate XMM-Newton and NuSTAR FPMA and FPMB spectra with the same summed (Epoch 3 + Epoch 4) net exposure times reported in Table 1. We adopt the same spectral grouping as described in Sect. 3. For each simulation, we first perform a fit in the range 3-10(3-30) keV for XMM-Newton(NuSTAR), ignoring the interval between 5 and 14 keV, to find the best-fit continuum and cold absorber parameters. Then, we freeze these parameters and we fit the WINE model (together with the two Gaussian absorption lines and the photoelectric edge), considering also the energy interval 5-14 keV.

Table 5, first column, reports the differences Δ between the input values and the results, according to the formula

$$\Delta = \frac{|V_i - \bar{V}_{out}|}{\sigma_{out}}, \quad (11)$$

where V_i is the input value, \bar{V}_{out} is the mean of the distribution of the best-fit values from 100 simulated spectra, and σ_{out} is the standard deviation of the distribution. The agreement between the mean values and the input parameters is remarkably good. We then perform an additional set of simulations, using different arbitrary input values, to check the capability of the WINE

Parameter	Value
<i>smedge</i>	
E (keV)	9.28 ^(f)
$z^{(a)}$	$-0.063^{+0.004}_{-0.005}$
$f^{(b)}$	0.23 ± 0.05
$index^{(c)}$	$-2.67^{(f)}$
$width^{(d)}$ (keV)	$0.60^{+0.08}_{-0.09}$
WINE model	
v_{max} (c)	$0.285^{+0.006}_{-0.007}$
s	$0.39^{+0.03}_{-0.04}$
θ_{out} (deg)	71^{+13}_{-8}
i (deg)	63^{+13}_{-16}
$K^{(e)(g)}$ (Ly α)	$1.2^{+0.3}_{-0.2} \times 10^{-7}$
$K^{(e)(g)}$ (Ly β)	$2.28^{+0.6}_{-0.3} \times 10^{-8}$
z	$0.184^{(f)}$
$v_{min}^{(h)}$ (c)	0.17 ± 0.01
$C_f^{(i)}$	$0.7^{+0.2}_{-0.1}$
<i>zgauss_Lyα</i>	
E (keV)	6.97 ^(f)
$\sigma^{(d)}$ (keV)	$0.45^{+0.06}_{-0.07}$
$z^{(a)}$	$-0.063^{+0.004}_{-0.005}$
$K^{(e)}$	$1.28 \pm 0.2 \times 10^{-5}$
<i>zgauss_Lyβ</i>	
E (keV)	8.25 ^(f)
$\sigma^{(d)}$ (keV)	$0.54^{+0.07}_{-0.08}$
$z^{(a)}$	$-0.063^{+0.004}_{-0.005}$
$K^{(e)}$	$4.0^{+0.6}_{-0.7} \times 10^{-6}$
$\chi^2/\text{d.o.f.}$	652/715

Table 4: Best-fit values for the absorption and emission components using the WINE model (see relation 8). ^(a) Redshift of the absorption components are linked. ^(b) f is defined as the absorption depth at threshold. ^(c) Photoelectric cross-section index. ^(d) Linked values. ^(e) Normalizations in units of total photons $\text{cm}^{-2} \text{s}^{-1}$. ^(g) WINE model normalizations are linked according to the ratio of the Ly α and Ly β oscillator strengths. ^(h) Derived minimum velocity of the wind (i.e., $v(r)$ for $r = 0$ and $r = r_{cone}$). ⁽ⁱ⁾ Derived opening angle of the cone. ^(f) Fixed value.

model to discriminate between different scenarios. Columns 2 and 3 of Table 5 report the input values and the resulting Δ , respectively.

Parameter	Model 1 ^(a)	Model 2 ^(b)	
	Δ	Input	Δ
v_{max}	0.07	0.35 c	0.05
s	0.37	0.7	0.21
θ_{out}	0.27	45 deg	0.31
i	0.44	4.5 deg	0.47
Derived qts. ^(c)			
v_{min}	0.36	0.10 c	0.21
C_f	0.30	0.29	0.26

Table 5: ^(a) Difference Δ between input values and results (see Eq. 11). Input parameters are those reported in Table 4). ^(b) Different arbitrary input values (center column) and corresponding Δ (right column). ^(c) These quantities are derived from the fit parameters, as described in Sect. 2.

4. Discussion

Using the novel wind emission (WINE) model, we constrained the velocity (mean value $\sim 0.23c$), opening angle (71 deg), and covering fraction (0.7) of the UFO in the quasar PDS 456. The results of our analysis are in agreement with the estimates on the bulk wind velocity and C_f in N15. For the first quantity they estimated $\sim 0.25c$, which is inside our radial excursion ($0.17 - 0.28c$).

The covering fraction in N15 is evaluated in different ways. The normalization of the XSTAR wind emission tables yields an average value between all the observations of $C_f = 0.8 \pm 0.1$, while the fraction of the absorbed continuum luminosity re-emitted by the wind gives $C_f > 0.5$.

We find a wind opening angle of 71^{+13}_{-8} deg, implying $C_f = 0.7^{+0.2}_{-0.1}$. This value is consistent with N15 and with UFO detection rates in the larger AGN population (see, e.g., Tombesi et al. 2010, Gofford et al. 2013, Tombesi et al. 2014).

Covering fraction is a key property in the calculation of the mass outflow rate, as expressed in Crenshaw & Kraemer (2012),

$$\dot{M}_{out} = 4\pi r N_H \mu m_p C_f v, \quad (12)$$

with r the launching radius, μ the mean atomic mass per proton (≈ 1.2 , Gofford et al. 2015), m_p the proton mass, and v the outflow velocity. From \dot{M}_{out} and v , it is possible to estimate the momentum rate, $\dot{P}_{out} = \dot{M}_{out}v$, and the energy transfer rate, $\dot{E}_{out} = \frac{1}{2}\dot{M}_{out}v^2$. These quantities are fundamental in the determination of the AGN feedback towards the host galaxy, and hence of their coupled evolution.

For the outflow velocity, we use $v = (0.23 \pm 0.06)c$, that is, the average velocity of the UFO v_{avg} as the mean value, and v_{max} and v_{min} (i.e., $v(r_{cone})$) as upper and lower limit, respectively. Moreover, we consider our covering fraction $C_f = 0.7$, while the following quantities are taken from N15: $N_H = 6 \times 10^{23} \text{ cm}^{-2}$, $r = 100r_g (= 1.5 \times 10^{16} \text{ cm})$, $L_{bol} \sim 10^{47} \text{ erg s}^{-1}$, and the black hole mass $M_{BH} = 10^9 M_\odot$. We find $\dot{M}_{out} \sim 16 \pm 4 M_{sun} \text{ yr}^{-1} \sim 0.23 \pm 0.06 \dot{M}_{Edd}$, for a radiative efficiency $\eta = 0.3$, as expected for luminous quasars such as PDS 456 (see, e.g., Davis & Laor 2011, Trakhtenbrot 2014). We derive a momentum rate $\dot{P}_{out} = 7 \pm 3 \times 10^{36} \text{ dyne}$, $\sim 2.1 \pm 1.1$ times the radiation momentum rate $\dot{P}_{rad} = L_{bol}/c$, and an energy rate $\dot{E}_{out} = 3 \pm 2 \times 10^{46} \text{ erg s}^{-1}$, that is, $\sim 30 \pm 20\% L_{AGN}$.

The average values for \dot{M}_{out} and \dot{E}_{out} are a factor of ~ 1.5 and ~ 1.3 times greater than that found in N15, respectively. This is mainly due to the different covering fractions (0.7 versus 0.5) and because they assume $\mu \equiv 1$ (i.e., the gas is composed only by hydrogen).

To investigate the possibility that the quality of the observations did not allow us to constrain the presence of an inner cavity, we run a set of 100 simulations of observation with the X-ray Integral Field Unit (X-IFU) instrument of the Advanced Telescope for High-Energy Astrophysics (ATHENA) (Nandra et al. 2013). We adopt the best fit model (see 8 and Table 4), including an internal cavity with angular amplitude $\theta_{in} = 21$ deg, the 90% upper limit reported in Sect. 3.2. We find that 500 ks are necessary to constrain the presence of the cavity, with a confidence level of 90%. With this exposure time we can measure the parameters with an accuracy higher than 6%, except for θ_{in} and C_f , for which the relative uncertainties are 18% and 11%, respectively. Further details are in Appendix A.

The results of this work show the robustness of the WINE model and its utility to constrain the properties of the outflow. This could be useful especially for those cases in which

it is not clear whether the emission and/or absorption features are mainly due to disk reflection or nuclear winds (see, e.g., Kouichi et al. 2016 for 1H 0707-495 and de La Calle Pérez et al. 2010, Patrick et al. 2012 for type I AGNs). More generally, this model represents a physically and geometrically based approach to explore outflow kinematics and can shed new light also on known UFOs from quasar sources (see, e.g., Kouichi et al. 2017, Parker et al. 2017, Tombesi et al. 2017). With some minor changes, this model can be applied also to larger scale outflows, such as broad line regions (BLRs) (Vietri et al. 2018) up to galactic-scale outflows (Feruglio et al. 2015).

In the forthcoming version of the WINE model we will use the XSTAR code to calculate the ionic abundances and emissivities. This will allow us to accurately take into account all the relevant transitions as a function of the density and the ionization parameter of the wind. We will also be able to constrain the launching radius and the spatial extent of the wind. Accordingly, the next version of the model will self-consistently represent both the emission and absorption features.

Acknowledgements. We thank the referee for useful comments and suggestions that helped improve the quality and the presentation of the paper. EP and LZ acknowledge financial support from the Italian Space Agency (ASI) under the contract ASI-INAF I/037/12/0 (NARO): “The unprecedented NuSTAR look at AGN through broadband X-ray spectroscopy”. FT acknowledges support by the Programma per Giovani Ricercatori - anno 2014 “Rita Levi Montalcini”. We thank Dr. K. Fukumura for helpful discussions.

References

- Bischetti et al., 2017, A&A, 598, A122
 Blandford & Payne, 1982, MNRAS, 199, 883
 de La Calle Pérez et al., 2010, A&A, 524, A50
 Crenshaw & Kraemer, 2012, ApJ, 753, 1, 75
 Davis & Laor, 2011, ApJ, 728, 98
 Di Matteo et al., 2005, Nature 433, 604
 Ebisawa et al. 1994, PASJ, 46, 375
 Elvis, 2000, ApJ, 545, 63-76
 Faucher-Giguère & Quataert, 2012, MNRAS, 425, 605
 Feruglio et al., 2015, A&A. 583, A99
 Fiore et al., 2017, A&A, 601, A143
 Fukumura et al., 2010, ApJ, 715, 1
 Fukumura et al., 2014, ApJ, 780, 2, 120
 Gofford et al., 2013, MNRAS, 430, 1, 60-80
 Gofford et al. 2015, MNRAS, 451, 4169
 Kallman & Bautista, 2001, ApJS, 133, 221
 Kazanas et al., 2012, Astron. Rev., 7, 3
 King & Pounds, 2015, Ann. Rev. Astron. and Astrophys, 53, 115-154
 Kormendy & Ho, 2013, ARAA, 51, 1, 511-653
 Kouichi et al., 2016, MNRAS, 461, 4
 Kouichi et al., 2017, MNRAS, 468, 2
 Molendi et al., 2003, MNRAS, 343, L1
 Nandra et al., 2013, arXiv:1306.2307
 Nardini et al., 2015, Science, 347,6224, 860-863
 Oshuga et al., 2009, PASJ, 61, 3, L7-L11
 Parker et al., 2017, NATURE, 543, 7643
 Patrick et al., 2012, MNRAS, 426,3
 Proga & Kallman, 2004, ApJ, 616, 2, 688-695
 Reeves et al., 2003, ApJ, 593, L65
 Reeves et al., 2009, ApJ, 701, 1
 Tombesi et al., 2010, A&A, 521, A57
 Tombesi et al., 2011, ApJ, 742, 1
 Tombesi et al., 2014, MNRAS, 443, 3, 2154-2182
 Tombesi et al., 2015, Nature, 519, 7544
 Tombesi et al., 2017, ApJ, 850, 2
 Trakhtenbrot, 2014, ApJL, 789, 1, L9
 Vietri et al., 2018, A&A accepted, <https://arxiv.org/abs/1802.03423>
 Zubovas & King, 2012, ApJL, 745, L34

Appendix A: ATHENA simulations

In order to assess the capability of the next-generation X-ray observatory ATHENA (Nandra et al. 2013) to constrain the presence of an internal cavity, we run a series of simulations with the X-IFU instrument³, using variable exposure times. We adopt the best-fit model found in Sect. 3.2, including also a cavity with $\theta_{in} = 21 \text{ deg}$, the 90% upper limit estimated in Sect. 3.2. We simulate a set of 100 spectra. For each one, we group the spectrum to a minimum of 100 counts per bin; then, we perform two different spectral fittings of the data, in the energy range 3–12 keV. In the first one, we assume a full cone geometry and in the second one we include the inner cavity. Finally, we perform the F-test to check if the difference in the statistics of the two fits is enough to justify the introduction of the cavity. We verify that an exposure time of 500 ks ensures that 90% of the simulated spectra allows us to discriminate the presence of the cavity with an F-test probability $< 1\%$.

Table A.1 reports the mean and the standard deviation of the distribution of the best-fit values using an exposure of 500 ks. Figure A.1 reports one of the simulated 500 ks spectra along with the best-fit inner cavity model.

Parameter	Input ^(a)	Results ^(b)
v_{max} (c)	0.285	0.285 ± 0.003
s	0.39	0.38 ± 0.01
θ_{out} (deg)	71	66 ± 4
i (deg)	63	62 ± 3
θ_{in} (deg)	21	22 ± 4
Derived qts. ^(c)		
v_{min} (c)	0.174	0.176 ± 0.005
C_f	0.60	0.53 ± 0.06

Table A.1: ^(a) Input values. ^(b) Mean \pm standard deviation for the distribution of the best-fit values for the 100 simulated spectra, with an observation time of 500 ks. ^(c) These quantities are derived from the fit parameters, as described in Sect. 2.

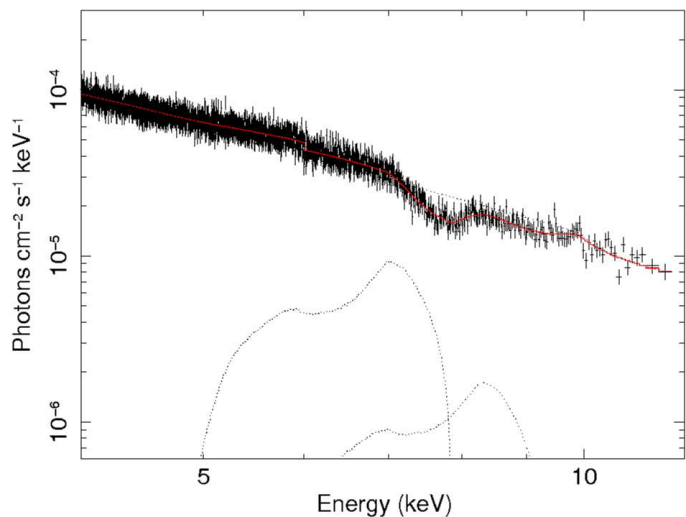


Fig. A.1: Particular of one of the ATHENA X-IFU 500 ks simulated spectrum, along with the best-fit model including an inner cavity (solid red line). The two $\text{Ly}\alpha$ and $\text{Ly}\beta$ WINE model components are reported as dotted lines.

³ We use response files and background spectra available at <http://x-ifu.irap.omp.eu/resources-for-users-and-x-ifu-consortium-members/>. We simulate the case of a mirror module radius of 1469 mm and adopt a background spectrum for an extraction area of 5 arcsec radius.